

Tuning the bandstructure of electrons in a two-dimensional artificial electrostatic crystal in GaAs quantum wells

Daisy Q. Wang,^{1,2} Zeb Krix,^{1,2} Olga A. Tkachenko,³ Vitaly A. Tkachenko,^{3,4} Chong Chen,⁵ Ian Farrer^{a,5} David A. Ritchie,⁵ Oleg P. Sushkov,^{1,2} Alexander R. Hamilton,^{1,2} and Oleh Klochan^{1,2,6}

¹*School of Physics, University of New South Wales, Kensington, NSW 2052, Australia*

²*Australian Research Council Centre of Excellence in Future Low-Energy Electronics Technologies, The University of New South Wales, Sydney 2052, Australia*

³*Rzhanov Institute of Semiconductor Physics, Novosibirsk, 630090, Russia*

⁴*Novosibirsk State University, Novosibirsk, 630090, Russia*

⁵*Cavendish Laboratory, J. J. Thomson Avenue, Cambridge, CB3 0HE, United Kingdom*

⁶*School of Science, The University of New South Wales, Canberra, ACT 2612, Australia*

(Dated: February 21, 2024)

arXiv:2402.12769v1 [cond-mat.mes-hall] 20 Feb 2024

^a Present Address: Department of Electronic and Electrical Engineering, The University of Sheffield, Mappin Street, Sheffield, S1 3JD, United Kingdom.

The electronic properties of solids are determined by the crystal structure and interactions between electrons, giving rise to a variety of collective phenomena including superconductivity, strange metals and correlated insulators. The mechanisms underpinning many of these collective phenomena remain unknown, driving interest in creating artificial crystals which replicate the system of interest while allowing precise control of key parameters. Cold atoms trapped in optical lattices provide great flexibility and tunability [1, 2], but cannot replicate the long range Coulomb interactions and long range hopping that drive collective phenomena in real crystals. Solid state approaches support long range hopping and interactions, but previous attempts with laterally patterned semiconductor systems were not able to create tunable low disorder artificial crystals, while approaches based on Moiré superlattices in twisted two-dimensional (2D) materials [3, 4] have limited tunability and control of lattice geometry. Here we demonstrate the formation of highly tunable artificial crystals by superimposing a periodic electrostatic potential on the 2D electron gas in an ultra-shallow (25 nm deep) GaAs quantum well. The 100 nm period artificial crystal is identified by the formation of a new bandstructure, different from the original cubic crystal and unique to the artificial triangular lattice: transport measurements show the Hall coefficient changing sign as the chemical potential sweeps through the artificial bands. Uniquely, the artificial bandstructure can be continuously tuned from parabolic free-electron bands into linear graphene-like and flat kagome-like bands in a single device. This approach allows the formation arbitrary geometry 2D artificial crystals, opening a new route to studying collective quantum states.

A key challenge in condensed-matter physics is understanding strongly interacting quantum systems, where many-body correlated states such as superconductivity emerge. Artificial crystals where the key parameters can be controlled in-situ can provide a powerful tool to simulate and study these complex systems. Compared to optical systems, the pioneer in the field of artificial crystals, solid-state based artificial crystals exhibit a pivotal advantage: easy integration of the long-range Coulomb interactions that are critical to emulating collective behaviour in real materials. However creating solid state artificial crystals is non-trivial. The major challenges lie in fabricating a highly uniform periodic potential $U(r)$ with an amplitude much larger than the Fermi energy E_F , while maintaining very low levels of disorder $\Gamma \ll U$.

Artificial solid state crystals have been explored in doped semiconductor heterostructures where nanolithography techniques allows lattices of arbitrary geometry to be created with excellent con-

trol. Early studies of one-dimensional lateral superlattices revealed periodic magnetoresistance oscillations when the electron's cyclotron orbit matches the 1D lattice spacing [5, 6], and in two dimensional lattices signatures of Hofstadter physics were observed [7–9]. However the weak artificial lattice potential ($U(r) \ll E_F$) and disorder prevented the formation of an artificial solid state crystal with different bandstructure and electronic properties than the host semiconductor. Optical studies of honeycomb lattices etched into GaAs quantum wells [10, 11] have revealed characteristics of the honeycomb bands [12], although etched systems do not allow tuning of the lattice potential, making it difficult to unambiguously identify the bandstructure. More recently periodic lattice potentials have been created by stacking and twisting two layers of atomically thin materials relative to one another [13, 14], revealing a rich variety of correlated electronic phases [15–18]. Despite these advances, these Moiré systems face their own set of challenges: the symmetry and strength of the artificial lattice potential are constrained by the host crystal, while twist angle disorder remains a difficult obstacle to overcome [19].

In this work we demonstrate a new route to creating low-disorder two-dimensional artificial crystals in semiconductor systems through electrostatic gating. Electron beam lithography is used to define a 100 nm period triangular lattice in a metal gate electrode only 25 nm above the electrons in a GaAs quantum well. This setup substantially amplifies the superlattice potential, allowing us to reach the regime where $U(r) \gg E_F$, while we eliminate random disorder from dopant atoms by using entirely undoped crystals so $\Gamma \ll E_F, U$. We detect formation of the artificial crystal by probing its unique bandstructure, with low-field transport measurements of the Hall effect directly revealing electron-like and hole-like charge carriers in the artificial bands. Independent confirmation of the formation of the artificial crystal comes from the magnetoresistance at higher magnetic field, which shows periodic oscillations as individual flux quanta are threaded through the artificial unit cell. Remarkably we can continuously tune the energy bands of the artificial crystal from the original parabolic free-electron dispersion to graphene-like and kagome-like bands in a single device, with signs of a correlated insulating state in the kagome flat band regime. We highlight that this electrostatic gating technique is not material specific: here it is demonstrated with GaAs/Al_{0.6}Ga_{0.4}As heterostructures, but it can be used with a multitude of semiconductors and atomically thin 2D materials. In the future it could be used to engineer artificial solid state crystals to study collective quantum phenomena such as correlated insulators, superconductivity, and magnetism in lattices of arbitrary geometry.

CALCULATING THE BANDSTRUCTURE OF THE ARTIFICIAL CRYSTAL

Determining the unique band structure of the artificial crystal is crucial for understanding its electronic properties. We thus begin with a comprehensive analysis of the 2D band structure and corresponding Fermi surface topology, which highlights the importance of a strong superlattice potential. Our experiments use a high-quality GaAs/Al_{0.6}Ga_{0.4}As heterostructure with a two-dimensional electron gas (2DEG) subjected to a periodic triangular anti-dot potential. A double-layer gate architecture, shown schematically in Fig. 1(a) and detailed in the Methods, allows independent control over the amplitude of superlattice potential and the electron density (the doping). We choose a triangular symmetry of the lattice potential since this creates a unique bandstructure that can be detected in measurements.

We model the electrostatic potential as a periodic potential shown in Fig. 1(b)) and described by Eqn. 1 in Methods (self consistent numerical modelling has also been performed in Refs. [20, 21]). We perform an exact numerical solution of the single-particle Schrödinger equation to obtain the artificial bandstructure. The key parameter that determines the effective strength of the periodic potential is the peak-to-peak magnitude U_{p-p} with respect to the Fermi energy E_F , as sketched in Fig. 1(b). When the superlattice potential is weak the mini-bands are essentially parabolic (Fig. 1(c)), corresponding to nearly-free electrons, a regime that has been studied extensively in experiments with GaAs superlattices [7–9, 22]. To create an artificial crystal it is necessary for the superlattice potential to be strong ($U_{p-p} \gg E_F$). In this regime (Fig. 1(e)) the energy bands become non-overlapping with two graphene-like bands at low energies (red) and three kagome-like bands (blue) at higher energies (by ‘graphene-like’ and ‘kagome-like’ we mean that the energy dispersion matches that of the corresponding lattice with nearest neighbour hopping). The major difference between the artificial bands in Fig. 1(e) and those in natural materials is the smaller bandwidth (meV instead of eV) due to the larger lattice constant, $a = 100$ nm. This necessitates very low levels of disorder, but means that the Fermi level can easily be swept through the different bands simply by tuning the bias on the patterned gate.

To understand the dynamics of electrons in this artificial crystal we look at the change in the Fermi surface topology as the bands are filled: if the Fermi surface expands as energy increases then charge carriers are electron-like, while if the Fermi surface shrinks then charge carriers are hole-like. The full bandstructure for a strong superlattice potential is shown in Fig. 1(f). Charge carriers can change from electron-like to hole-like (or vice versa) only at certain points in the band structure: at van Hove singularities or at Dirac points, labelled in Fig. 1(f) as VH and DP, respectively. The

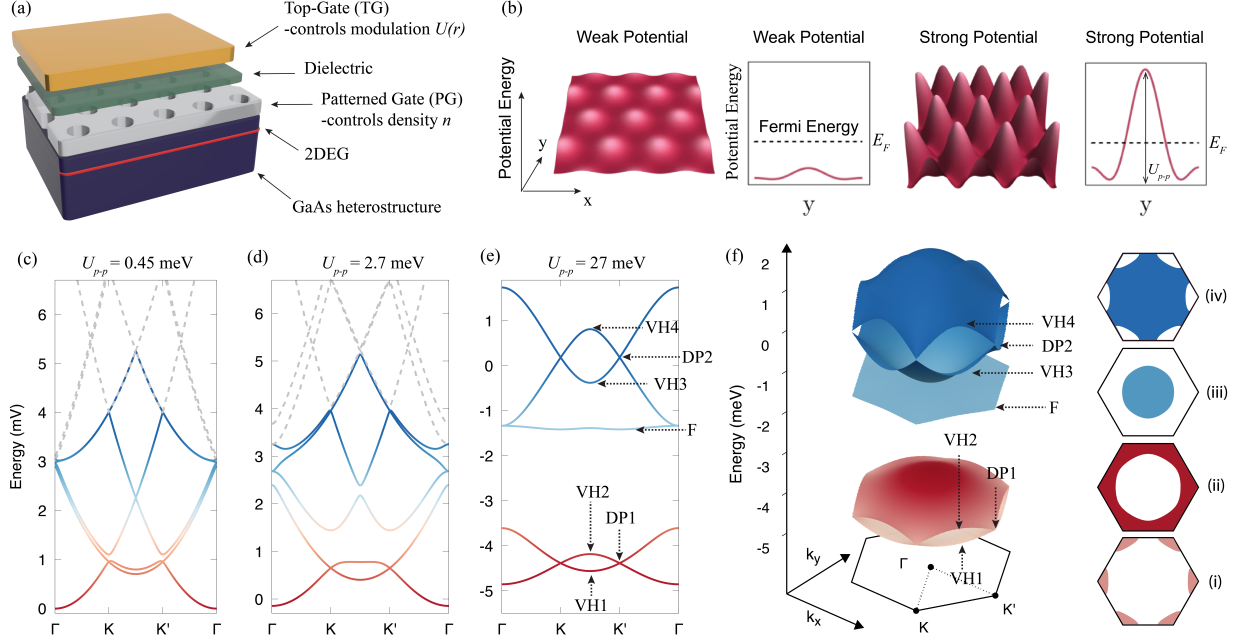


FIG. 1. Bandstructure of the artificial crystal. The system we consider is a two-dimensional electron system in a GaAs/Al_{0.6}Ga_{0.4}As quantum well with a periodic potential imposed on it. A strong modulation potential $U(r)$ is essential for creating an artificial crystal with a well defined bandstructure. (a) Schematic of the device, showing the double-layer gate design. A surface metal patterned gate (PG, closest to the 2DEG) is patterned with a triangular array of holes and positively biased to induce electrons at the heterointerface 25 nm below the gate. The lattice constant is $a = 100$ nm and the hole diameter is 45 nm. The overall top gate (TG), separated by a thin AlO_x dielectric, controls the strength of the superlattice potential through the holes etched in the patterned gate. (b) The modulation potential in the weak $U_{p-p} < E_F$ and strong ($U_{p-p} > E_F$) limits. (c, d, e) Evolution of the calculated bandstructure for a 100 nm lattice spacing with different peak-to-peak modulation amplitudes U_{p-p} . (c) For a weak modulation potential ($U < E_F$, typically $E_F \sim 2.5$ meV), the mini-bands have mostly parabolic energy dispersion, with small splittings near the artificial Brillouin zone boundary. (d) As the strength of the modulation potential increases the splittings at the zone boundaries become larger, although only the lowest bands are well defined; higher bands overlap and form a 'spaghetti' of intersecting levels. (e) Only at very strong potential modulation do the mini-bands become distinct and non-overlapping, with a set of two graphene-like bands at lower energies (red), and three kagome-like bands at higher energies (blue). Special points in the bandstructure can be identified in experiments: the van Hove singularities at the band edges (VH1-VH4), the Dirac points at band crossings (DP1 and DP2), and also the flat band (F). (f) A surface plot of the bandstructure in (e), and cross-sectional plots of the Fermi surfaces (i), (ii), (iii) and (iv), show how the carriers in the artificial bands change from electron-like to hole-like as the Fermi energy is increased. The shaded regions in panels (i)-(iv) indicate occupied momentum states. (i) Fermi energy is between DP1 and VH2 (electron-like carriers). (ii) The Fermi energy is just above VH2 (hole-like carriers). (iii) Fermi energy is between F and VH3 (electron-like carriers). (iv) Fermi energy is between VH3 and DP2 (hole-like carriers).

insets (i-iv) of Fig. 1(f) show the Fermi surfaces between these special points, with shaded areas corresponding to occupied states. Panels (i) and (iii) show an electron-like Fermi surface, while panels (ii) and (iv) show a hole-like Fermi surface. A key experimental signature of the artificial crystal will be to detect transitions between electron-like and hole-like behaviour.

MEASURING THE ARTIFICIAL BANDSTRUCTURE

Experimentally we probe the formation of the artificial bandstructure using measurements of the low-field magnetoresistance at $T = 1.5$ K (Fig. 2). The sample has a Van der Pauw geometry with approximately 2,600 lattice sites which allows four terminal measurements of the longitudinal R_{xx} and transverse (Hall) R_{xy} resistances as a function of magnetic field and gate biases. The superlattice potential is controlled with a negative bias V_{TG} on the top-gate, while the carrier density, or band filling, is proportional to the positive bias V_{PG} on the patterned gate. The sign of the Hall slope probes whether charge carriers are electron-like or hole-like, and can hence detect the formation of artificial bands. We highlight that the results are highly reproducible, not only between devices made on the same heterostructure, but even between devices made with different lattice constants and from different wafers (Supplementary section III).

When the superlattice potential is weak the system behaves as a conventional 2DEG. In this well-explored regime [5, 22] the Hall resistance is featureless over the entire range of 2DEG density, with a negative Hall slope $R_H = dR_{xy}/dB$ indicating that charge carriers are electron-like (Fig. S1 of Supplementary section I). To create the artificial crystal we increase the strength of the superlattice potential by making V_{TG} more negative. The formation of the artificial crystal modifies the Hall effect: the carriers change behaviour from electron-like to hole-like as the Fermi energy is swept through the artificial bands, causing a change in sign of the Hall coefficient as V_{PG} is increased (Fig. 2(a,b,c)). The observation of a positive Hall slope is an unambiguous signature of hole-like carriers, which can only arise due to the formation of mini-bands in the artificial crystal.

The measured Hall coefficient in Fig. 2(c) is related to the calculated bandstructure by counting the number of transitions between electron-like ($R_H < 0$, blue) and hole-like ($R_H > 0$, red) behaviour with increasing carrier density. These transition points must correspond to either a van Hove singularity (VH) or a Dirac point (DP). We observe four regions of different carrier type in Fig. 2(c), with three transitions, which match well with the VH1, DP1, and VH2 points in the calculated band diagram (Fig. 2(d)). For high densities (above the last hole-like region, $V_{PG} > 0.875$ V) R_H is strongly suppressed as the mini-bands merge together into a continuum at

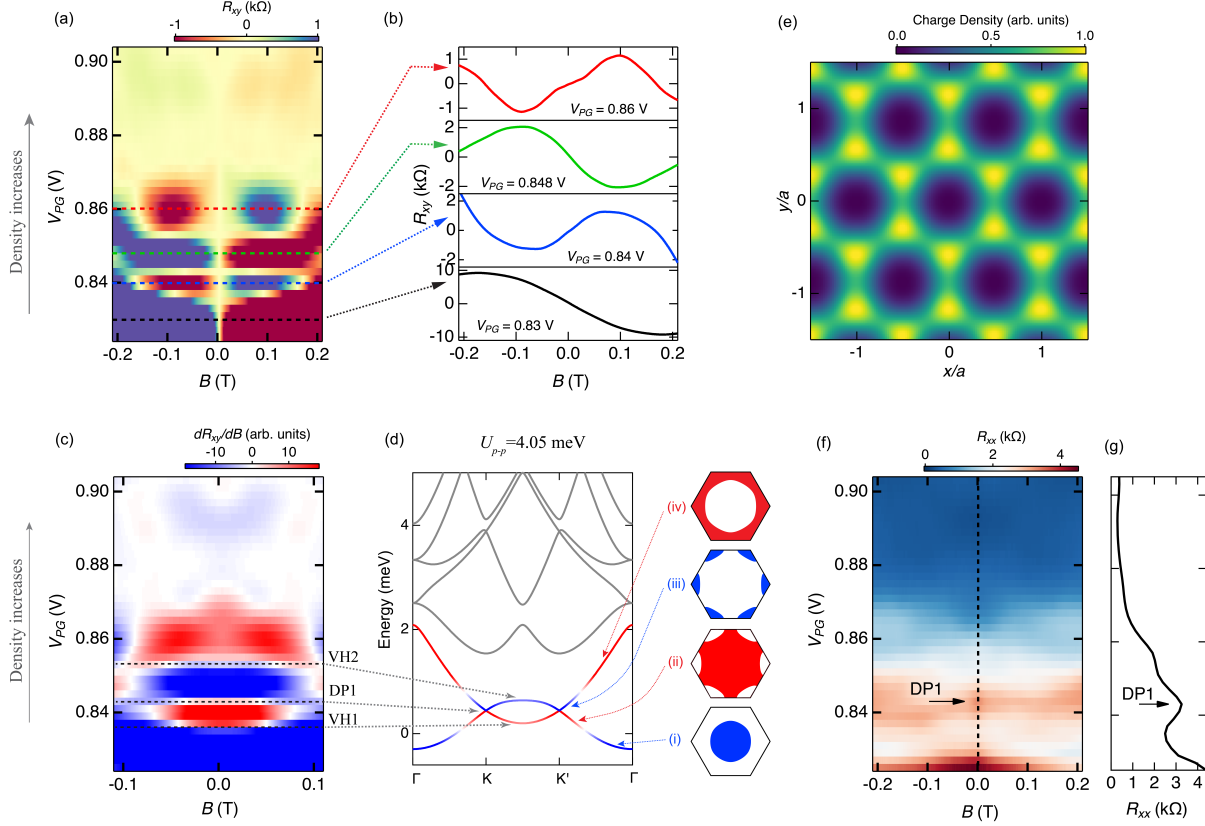


FIG. 2. Measuring artificial bandstructure in graphene-like bands. The 100 nm period triangular superlattice imposed by the negative bias $V_{TG} = -0.5$ V on the top-gate causes the electrons in the host semiconductor to alternately behave as electrons and holes as the Fermi energy is swept through the artificial bands. This provides unique features in the low field Hall effect and the longitudinal resistance measured at $T = 1.5$ K. (a) In contrast to the host semiconductor the low field Hall resistance R_{xy} is no longer featureless, but shows striking features as a function of V_{PG} (proportional to the 2DEG density) and magnetic field, B . (b) Line cuts of the Hall resistance at four different carrier densities indicated by the dashed lines in (a). The Hall slope changes sign near $B = 0$: the black and green lines have a negative slope indicative of electron-like carriers, while the red and blue lines have a positive slope indicative of hole-like carriers. The transition points between electron-like and hole-like behaviour are highlighted in panel (c), which shows a colour map of the Hall coefficient $R_H = dR_{xy}/dB$. Electron-like and hole-like behaviour is indicated by the colour (blue and red, respectively). Three transition points separate four regions of different carrier type, alternating between electron-like, hole-like, electron-like and hole-like as V_{PG} is increased. This sequence of transitions is consistent with the calculated band structure (panel (d)), where the two graphene-like bands at low energy have three transition points: VH1, DP1, and VH2. The electron-like (blue) and hole-like (red) behaviour on either side of a transition is colour-coded, with sub panels (i-iv) showing the corresponding Fermi surfaces. (e) The calculated charge distribution corresponding to $E_F = 1.5$ meV shows a honeycomb lattice. (f) Additional evidence for the formation of a Dirac point comes from the longitudinal resistance R_{xx} , plotted as a function of V_{PG} and magnetic field, B . A line cut of R_{xx} at $B = 0$ in panel (g) shows a clear resistance peak at the position of the Dirac point DP1 (indicated by the black arrow).

high energies $E_F \sim U_{p-p}$. We use this point at which R_H is suppressed to estimate the value of U_{p-p} (Supplementary section V).

Additional evidence for the formation of graphene-like bands comes from the evolution of the longitudinal resistance R_{xx} as a function of carrier density (controlled by V_{PG} , Fig. 2(f)). There is a clear resistance peak at $V_{PG} = 0.843$ V centered at the position of the Dirac Point DP1 (DP1 was previously identified from the sequence of the Hall coefficient sign changes). This resistance peak is expected for a graphene-like system. We estimate the mobility of the charge carriers near the artificial Dirac cone using the resistance and effective density at VH1 or VH2 ($0.6 \times 10^{10} \text{ cm}^{-2}$) to be $\mu_D \approx 100,000 \text{ cm}^2/\text{Vs}$, approximately 10 times higher than that of the host 2DEG at the same carrier density. This high mobility is consistent with the ‘massless’ nature of Dirac carriers in the graphene-like bands. We use the width of the Dirac peak to estimate the disorder, $\Gamma \approx 0.1 \text{ meV}$, which is 40 times smaller than the superlattice potential U_{p-p} .

Previous studies of gate defined artificial lattices were unable to reach the strong modulation regime $U_{p-p} \sim E_F$ without the system breaking up into ‘puddles’ due to long range disorder [23, 24]. Optical studies of honeycomb lattices etched into GaAs quantum wells have revealed signatures of linearly dispersing bands [12], but etched systems do not allow continuous tuning of the superlattice potential. In contrast, here we have tuned continuously from an unperturbed system with massive electrons in parabolic bands to electrons and holes in an artificial graphene bandstructure.

TUNING FROM GRAPHENE-LIKE TO KAGOME-LIKE BANDS

Having shown that we can use the electrostatic gate to transform the 2D electrons in the GaAs quantum well into holes and graphene-like particles we now exploit the ability to tune the strength of the superlattice potential to create a kagome lattice with flat bands. We continuously increase the modulation strength with V_{TG} and track the resulting evolution of the bandstructure through the experimentally determined transition points that separate the electron-like and hole-like behaviour (Supplementary Section II). As V_{TG} is made more negative, these transition points in the Hall resistance move to more positive V_{PG} . In Fig. 3(a) we show the measured Hall resistance at the strongest superlattice potential $V_{TG} = -3$ V (the most negative bias that could be applied while keeping the gate leakage below 0.1 nA). The increased modulation causes the sign changes of R_H associated with the VH1, VH2 and DP1 points in the lower graphene-like bands at low V_{PG} to be suppressed (although their evolution can be followed in Supplementary Section II), with new sign changes emerging at higher V_{PG} associated with the formation of well-defined kagome-like bands.

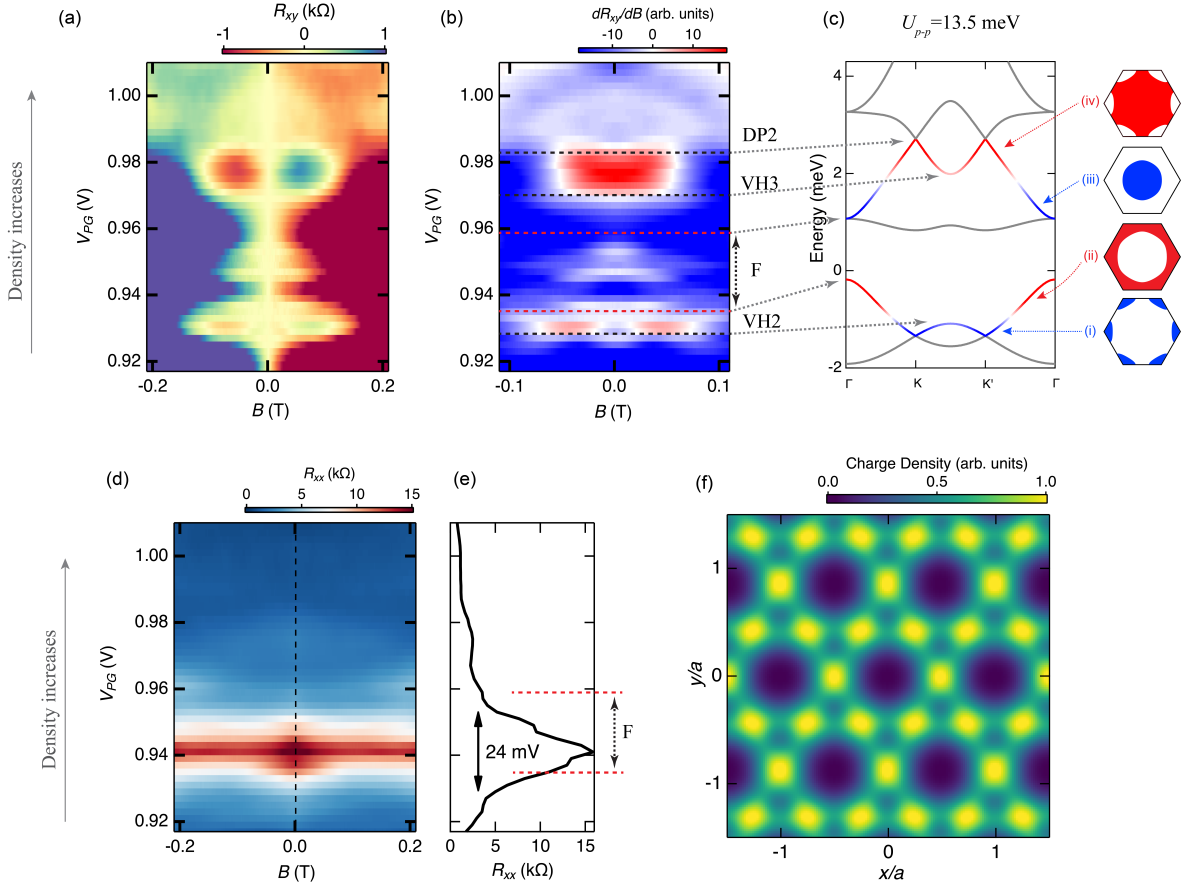


FIG. 3. Formation of kagome-like bands. The top-gate bias is increased to $V_{TG} = -3$ V to create a strong superlattice potential, $U_{p-p} \gg E_F$. (a) Measurements of the low field Hall effect show additional features in the colourmap of the Hall resistance R_{xy} at $V_{PG} > 0.94$ V due to the formation of kagome bands. (b) Transitions between electron-like (blue) and hole-like (red) Hall coefficient dR_{xy}/dB calculated from the data in (a) as the carrier density is tuned with V_{PG} . Black dashed lines indicate the positions of the special points VH2, VH3, and DP2 where the Hall coefficient changes sign. The red dashed lines demarcate the flat band region F where the Hall coefficient is not well defined theoretically. (c) The calculated bandstructure for $U_{p-p} = 13.5$ meV shows both graphene-like and kagome-like bands (see Supplementary Section V for details of the estimation of the superlattice potential and the effects of Coulomb screening due to filling of multiple bands). Insets show the Fermi surfaces, indicating either electron-like (blue) or hole-like (red) charge carriers as the bands are filled. Comparison with the measured Hall data in (b) give the width of a full band as $\Delta V_{PG} = 24$ mV. (d) The measured longitudinal resistance R_{xx} as a function of V_{PG} and magnetic field B shows an increased resistance in the flat band region F. (e) Longitudinal resistance as a function of V_{PG} at $B = 0$ (taken along the dashed line in panel (d)). A strong resistance peak occurs in the band gap and flat band region (red dashed lines demarcate the flat band F). This resistance peak is not due to sample disorder, since it disappears as the density is *decreased*. The width of the peak corresponds to filling a complete artificial band, $\Delta V_{PG} = 24$ mV, as indicated by the black arrows. (f) The calculated charge density distribution of the electron states integrated within the energy range 0.5 meV $< E < 2.7$ meV, see panel (c), shows the kagome lattice structure.

We relate the experimental data to theoretical calculations by mapping electron-like and hole-like regions of the Hall coefficient (Fig. 3(b)) to the calculated bandstructure in Fig. 3(c). This allows the identification of the second and third van Hove singularities VH2 and VH3, as well as the second Dirac point DP2. The change in V_{PG} from the top of the graphene-like bands to DP2 corresponds to filling two bands, which is used to extract the width of a single band $\Delta V_{PG} \approx 0.024$ V. This provides a calibration that will later be used to count how many artificial bands are filled for a given change in V_{PG} , and to locate the flat band region.

A key feature of the kagome-like bands is the flat band. Such bands often host correlated states as the kinetic energy is quenched. The calculated band diagram in Fig. 3(c) shows a well-developed flat band F with a width of ~ 0.25 meV separated from the lower graphene-like bands by a ~ 1 meV band gap. Using the method in Ref. [25] we estimate the ratio between Coulomb energy and kinetic energy in the upper kagome-like bands to be approximately 5. This implies that the upper kagome-like bands are still in the Fermi liquid regime. Within the flat band, however, the ratio between Coulomb and kinetic energy is enhanced by about 10 times due to its narrow bandwidth, meaning that the flat band is within the strongly correlated regime. Therefore, the Hall coefficient within the flat band is not defined by the single particle bandstructure and cannot be used to identify this band. We can see a signature of the flat band, however, in the longitudinal resistance R_{xx} (Fig. 3(d,e)). The resistance R_{xx} at $B = 0$ shows a strong peak, which starts from where R_{xy} identifies the position of the band-gap, and peaks at $V_{PG} = 0.941$ V in the flat band region. We emphasise that this resistance peak cannot be caused by a Mott-Anderson disorder transition unrelated to the artificial lattice, because the resistance drops from the peak value of 15 k Ω to 3 k Ω at both higher *and* lower carrier densities. In contrast trivial disorder would cause the resistance to always increase with decreasing carrier density. Furthermore, the width of the peak ≈ 0.024 V is consistent with the electron density required to fill one band noted previously. This suggests the peak is due to localisation of electrons in a band rather than a single particle insulator due to a band gap. The existence of this re-entrant resistance peak in the flat band region, together with the large ratio between Coulomb and kinetic energy, strongly hints toward correlation effects that could be of interest for future studies.

ARTIFICIAL CRYSTAL IN ULTRA-HIGH EFFECTIVE MAGNETIC FIELD

We provide additional confirmation of the formation of an artificial crystal by studying the magnetoresistance at higher magnetic fields. The large lattice constant in our system ($a = 100$

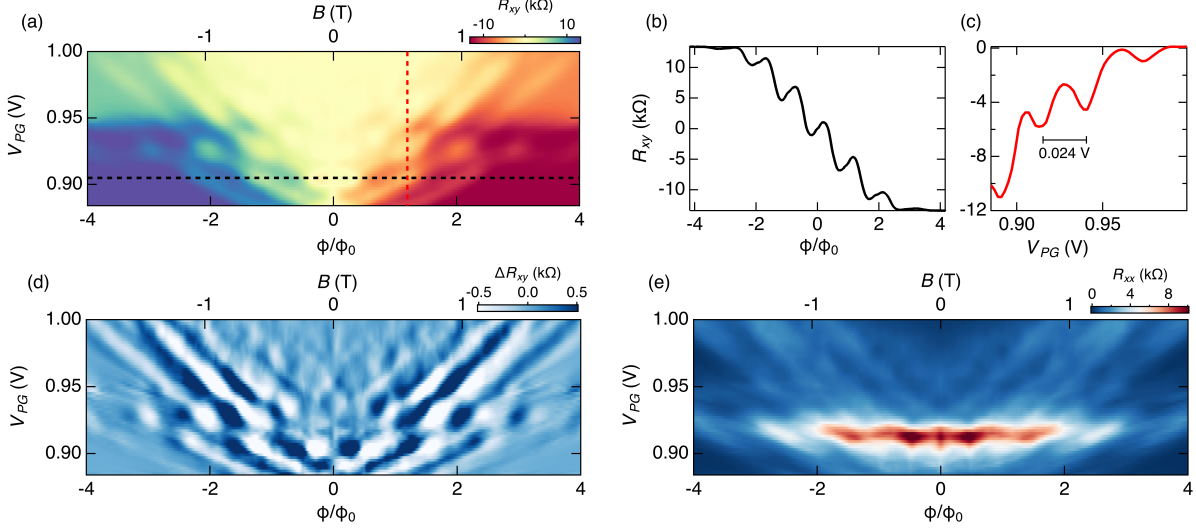


FIG. 4. **Magnetoresistance in the high magnetic field regime.** Data taken for a strong superlattice potential, $V_{TG} = -2$ V at $T = 1.5$ K show periodic features caused by the artificial lattice. Similar oscillations are also observed at higher V_{TG} . (a-c) The Hall resistance shows periodic oscillations both as a function of magnetic field and as a function of band filling controlled by V_{PG} . (a) Colour map of the Hall resistance R_{xy} as a function of V_{PG} and magnetic field in flux quanta per artificial unit cell Φ/Φ_0 (the equivalent magnetic field in Tesla is shown on the top axis). (b) Horizontal linecut of Hall resistance along the black dashed line in (a) showing oscillations with a period of one flux quantum per artificial unit cell. (c) Vertical linecut of Hall resistance along the red dashed line in (a) showing oscillations with period corresponding to the filling of one artificial band. This period $\Delta V_{PG} \approx 0.024$ V is consistent with the band assignments from Fig. 3. (d) The Hofstadter butterfly spectrum, and a phase shift in the Hall signal at $V_{PG} = 0.915$ V corresponding to the kagome flat band, are revealed by subtracting a slowly varying background from the Hall resistance in panel (a) to give ΔR_{xy} . (e) The colourmap of the longitudinal resistance R_{xx} as a function of V_{PG} and flux quanta per unit cell shows a resistance peak (red) corresponding to the kagome flat band, $V_{PG} \approx 0.915$ V.

nm) allows access to ultra-high effective magnetic fields with multiple flux quanta per unit cell ($\Phi/\Phi_0 = 1$, with $\Phi_0 = h/e$ corresponds to $B_0 = 0.48$ T), which is not possible in natural materials such as graphene (where $B_0 \approx 80,000$ T) or Moiré superlattices such as magic-angle twisted bilayer graphene ($B_0 \approx 30$ T). First, R_{xy} measured up to $B = 2$ T (Fig. S7(a,b)) shows oscillations which are periodic in the number of magnetic flux quanta per superlattice unit cell. The observation of oscillations with period $\Delta\Phi = \Phi_0$ proves that electrons are hopping between localised sites on the artificial lattice: gauge invariance requires that physical properties must be invariant under addition one flux quantum per unit cell for electrons on a lattice. Second, R_{xy} shows regular

oscillations in V_{PG} , with a period $\Delta V_{PG} = 0.024$ V (Fig. 3(c)). This periodicity perfectly matches the value obtained previously for the filling of one artificial mini-band, confirming that the features in the magnetoresistance with increasing V_{PG} correspond to electrons filling bands in the artificial lattice. This also validates the assignment of features in the experimental data to the theoretically calculated bandstructure in Figs. 2, 3. The measured data here is, with some exceptions noted below, in remarkably good agreement with numerical calculations of the energy spectrum presented in Supplementary section VII.

Finally we use the oscillatory magnetoresistance to probe the flat band region. To highlight the periodic pattern in R_{xy} (Fig. S7a) we subtract a slowly varying background to obtain ΔR_{xy} (Fig. S7(d)). This ΔR_{xy} reveals a distinct shift in the phase of the oscillations when carriers start to populate the flat band at $V_{PG} \approx 0.915$ V. Although the single-particle calculation described in Supplementary section VII perfectly reproduces the periodicities along Φ and V_{PG} it cannot explain the observed phase shift. Since the phase shift in ΔR_{xy} also coincides with the R_{xx} resistance peak in Fig. S7(e), it is plausible that both signatures are due to correlations, with charge carriers becoming immobilised as the kagome flat band is populated. These high magnetic field data confirm that it is possible to create artificial crystals where electron-electron interactions are much stronger than the disorder potential, which will enable the study of correlated states in arbitrary lattice geometries.

DISCUSSION

In this work we have established a new approach for creating solid state artificial crystals to allow studies of physical phenomena driven by long-range hopping and strong Coulomb interactions. Our approach exploits both the flexibility of electron beam lithography to create lattices of arbitrary geometry and a double-layer gate architecture that allows the amplitude of the superlattice potential and the chemical potential of electrons to be continuously tuned. Experimentally, we detected the artificial crystal via formation of a new bandstructure, with the Hall coefficient changing sign as the carrier behaviour alternated from electron-like to hole-like when the chemical potential was swept through the artificial bands. The artificial bandstructure was continuously tuned from parabolic free-electron bands into graphene-like and kagome-like bands simply by tuning a gate voltage. The experimental data was in excellent agreement with theoretical calculations of the predicted bandstructure. Further studies will be required to determine the exact nature of the re-entrant insulating phase in the kagome flat band regime, and the role of many-body

interactions.

We emphasise that our approach not only allows lattices of any geometry to be created, but is material agnostic and can be applied to a variety of 2D systems, including atomically thin materials [26–29]. Furthermore, the technique can be extended to create topological systems by introducing a spin-orbit interaction by using valence band holes instead of conduction band electrons [21], or to study exotic phases in honeycomb and kagome systems [30, 31] including ferrielectric and topological ferromagnetic states in the high magnetic field regime [32, 33]. Overall, the ability to create arbitrary crystal geometries, with unprecedented control over topology, doping, spin-orbit interaction, and superlattice potential will allow an enormous variety of systems to be fabricated and studied.

Acknowledgements This work was funded by the Australian Research Council Centre of Excellence for Future Low Energy Electronics Technologies (CE170100039) and EP/R029075/1 Non-Ergodic Quantum Manipulation, UK. Device fabrication was partially carried out at the Australian National Fabrication Facility (ANFF) at the UNSW node.

Author contributions D.Q.W. fabricated samples and performed transport measurements. D.Q.W., Z.K., O.P.S., A.R.H. and O.K. performed data analysis and discussed the results. A.R.H., O.P.S. and O.K. supervised the project. Z.K., O.P.S., O.A.T. and V.A.T. performed numerical calculations. C.C., I.F. and D.A.R. provided the GaAs/Al_{0.6}Ga_{0.4}As heterostructures. D.W., Z.K., O.P.S., A.R.H. and O.K. co-wrote the manuscript with input from all co-authors.

METHODS

Theoretical methods. To model the artificial crystal we need to know the shape of the potential experienced by electrons in the 2DEG. A full three-dimensional numerical model of the device in Fig. 1(a), including Hartree screening, has been used in Ref. [20] to calculate the artificial bandstructure. To simplify the analysis we construct a model Hamiltonian which depends on only a single parameter W which represents the amplitude of the applied potential, yet captures the essential physics and produces a bandstructure in very good agreement with the full 3D numerical solution:

$$\begin{aligned}
 H &= \frac{p^2}{2m^*} + U(\mathbf{r}) \\
 U(\mathbf{r}) &= 2W [\cos(\mathbf{G}_1 \cdot \mathbf{r}) + \cos(\mathbf{G}_2 \cdot \mathbf{r}) + \cos(\mathbf{G}_3 \cdot \mathbf{r})]
 \end{aligned}
 \tag{1}$$

Where $\mathbf{G}_{1,2}$ are the basic reciprocal vectors of the triangular lattice and $\mathbf{G}_3 = \mathbf{G}_2 - \mathbf{G}_1$ with $|\mathbf{G}_i| = 4\pi/\sqrt{3}a$. Note that the minimum of the potential is $U = -3W$ and the maximum is $U = 6W$, such that the peak-to-peak potential amplitude U_{p-p} is

$$U_{p-p} = 9W \quad (2)$$

The lattice constant a is 100 nm in all calculations. Here, higher harmonics of the potential have been neglected. The validity of this Hamiltonian has been checked against fully numerical 3D finite element Poisson calculations in Ref. [20]. It is possible, however, to understand the form of Eqn. 1 in terms of the following considerations: (i) at the level of the patterned gate the potential has the shape of a triangular array of (circular) hat functions. (ii) According to the Poisson equation, electrons in the plane of the 2DEG experience this potential with Fourier components modified from $U_k \rightarrow e^{-kz}U_k$, where z is the distance to the gate. (iii) The fundamental harmonics have the form $\cos(\mathbf{G}_i \cdot \mathbf{r})$, with $|\mathbf{G}| = 4\pi/\sqrt{3}a$, and higher harmonics are suppressed relative to these by a factor $e^{-4\pi/\sqrt{3}a} (\approx 0.1)$. (iv) For $W = 0$ electrons in the 2DEG are described by a quadratic dispersion, $p^2/2m^*$, where $m^* = 0.0667m_e$ is the effective mass of electrons in GaAs.

The band structures were computed by exact numerical diagonalisation of the Hamiltonian in Eqn. 1. To do this we write Eqn. 1 in the basis of plane wave states, $|\mathbf{k}\rangle = e^{i\mathbf{k}\cdot\mathbf{r}}$. Since $U(\mathbf{r})$ only mixes states which differ in momentum by $\pm\mathbf{G}_i$ or $\pm\mathbf{G}_2$ this basis can be restricted to states, $|\mathbf{k} + \mathbf{g}_i\rangle$, where \mathbf{k} is a momentum within the first Brillouin zone and \mathbf{g}_i is an arbitrary reciprocal lattice vector. We thus diagonalise the following matrix

$$\langle \mathbf{k} + \mathbf{g}_i | H | \mathbf{k} + \mathbf{g}_j \rangle = \frac{(\mathbf{k} + \mathbf{g}_i)^2}{2m} \delta_{ij} + W \sum_{n=1}^3 \delta(\mathbf{g}_i - \mathbf{g}_j - \mathbf{G}_n)$$

Where δ_{ij} is the Kronecker symbol. This matrix must be truncated such that the $|\mathbf{g}_i|$ are smaller than some upper limit; the limit is chosen such that eigenvalues and eigenvectors are independent of the limit (for example, the limit $\mathbf{g} = n\mathbf{G}_1 + m\mathbf{G}_2$ with $|n|, |m| \leq 10$ is more than large enough for the strongest potentials that we consider). Numerical diagonalisation gives a set of energy levels $\epsilon_n(\mathbf{k})$ (these are plotted in Fig. 1) and a set of corresponding Bloch functions $\psi_{n,\mathbf{k}}(\mathbf{r})$. The charge densities shown in Figs. 2e and 3f are equal to $\sum_{\mu_0 < \epsilon_n(\mathbf{k}) < \mu} |\psi_{n,\mathbf{k}}(\mathbf{r})|^2$. For Fig. 2e we sum over states from the bottom of band 1 to the mid-point of band 2 ($\mu = 1.5$ meV). For Fig. 3f we sum over states from the bottom of band 3 to the top of band 4, -0.5 meV $< \epsilon < 2.7$ meV. Of course, in the latter case, bands 1 and 2 also contribute to the total charge density, however, these states

are not physically relevant when μ is within the kagome-like bands and we exclude them for the sake of clarity.

Experimental methods. The devices in this study are fabricated on an ultra-shallow high quality undoped GaAs/Al_{0.6}Ga_{0.4}As heterostructure comprising of a 3 nm GaAs cap, a 22 nm AlGaAs layer, and a thick GaAs buffer layer, grown by molecular beam epitaxy. N-type ohmic contacts (AuGe) to the heterostructure were thermally evaporated into etched pits and then annealed. The triangular lattice is patterned into the surface metal gate by electron-beam lithography and reactive ion etching with SF₆. A 15 nm thick AlO_x is deposited via atomic layer deposition to isolate the metal gates from each other and from the ohmic contacts [34]. The mean free path of electrons in the unpatterned wafer is 3 μm at $n = 2 \times 10^{11} \text{ cm}^{-2}$, much larger than the lattice constant. Transport measurements were performed with standard lock-in techniques at 33 Hz. Both Hall and longitudinal resistance are measured in a Van der Pauw geometry over a patterned area of $5 \times 5 \mu\text{m}$.

REFERENCES

- [1] Leticia Tarruell, Daniel Greif, Thomas Uehlinger, Gregor Jotzu, and Tilman Esslinger, “Creating, moving and merging dirac points with a fermi gas in a tunable honeycomb lattice,” *Nature* **483**, 302–305 (2012).
- [2] N Goldman, J C Budich, and P Zoller, “Topological quantum matter with ultracold gases in optical lattices,” *Nature Physics* **12**, 639–645 (2016).
- [3] Dante M Kennes, Martin Claassen, Lede Xian, Antoine Georges, Andrew J Millis, James Hone, Cory R Dean, D N Basov, Abhay N Pasupathy, and Angel Rubio, “Moiré heterostructures as a condensed-matter quantum simulator,” *Nature Physics* **17**, 155–163 (2021).
- [4] Kin Fai Mak and Jie Shan, “Semiconductor moiré materials,” *Nature Nanotechnology* **17**, 686–695 (2022).
- [5] Dieter Weiss, KV Klitzing, K Ploog, and G Weimann, “Magnetoresistance oscillations in a two-dimensional electron gas induced by a submicrometer periodic potential,” *Europhysics Letters* **8**, 179 (1989).
- [6] R. W. Winkler, J. P. Kotthaus, and K. Ploog, “Landau band conductivity in a two-dimensional electron system modulated by an artificial one-dimensional superlattice potential,” *Phys. Rev. Lett.* **62**, 1177–1180 (1989).
- [7] C. Albrecht, J. H. Smet, D. Weiss, K. von Klitzing, R. Hennig, M. Langenbuch, M. Suhrke, U. Rössler, V. Umansky, and H. Schweizer, “Fermiology of two-dimensional lateral superlattices,” *Phys. Rev. Lett.* **83**, 2234–2237 (1999).

- [8] R. A. Deutschmann, W. Wegscheider, M. Rother, M. Bichler, G. Abstreiter, C. Albrecht, and J. H. Smet, “Quantum interference in artificial band structures,” *Phys. Rev. Lett.* **86**, 1857–1860 (2001).
- [9] M. C. Geisler, J. H. Smet, V. Umansky, K. von Klitzing, B. Naundorf, R. Ketzmerick, and H. Schweizer, “Detection of a landau band-coupling-induced rearrangement of the hofstadter butterfly,” *Phys. Rev. Lett.* **92**, 256801 (2004).
- [10] Marco Gibertini, Achintya Singha, Vittorio Pellegrini, Marco Polini, Giovanni Vignale, Aron Pinczuk, Loren N. Pfeiffer, and Ken W. West, “Engineering artificial graphene in a two-dimensional electron gas,” *Phys. Rev. B* **79**, 241406 (2009).
- [11] A. Singha, M. Gibertini, B. Karmakar, S. Yuan, M. Polini, G. Vignale, M. I. Katsnelson, A. Pinczuk, L. N. Pfeiffer, K. W. West, and V. Pellegrini, “Two-dimensional mott-hubbard electrons in an artificial honeycomb lattice,” *Science* **332**, 1176–1179 (2011).
- [12] Sheng Wang, Diego Scarabelli, Lingjie Du, Yuliya Y. Kuznetsova, Loren N. Pfeiffer, Ken W. West, Geoff C. Gardner, Michael J. Manfra, Vittorio Pellegrini, Shalom J. Wind, and Aron Pinczuk, “Observation of dirac bands in artificial graphene in small-period nanopatterned gaas quantum wells,” *Nature Nanotechnology* **13**, 29 (2018).
- [13] A K Geim and I V Grigorieva, “Van der waals heterostructures,” *Nature* **499**, 419–425 (2013).
- [14] Eva Y Andrei and Allan H MacDonald, “Graphene bilayers with a twist,” *Nature Materials* **19**, 1265–1275 (2020).
- [15] Yuan Cao, Valla Fatemi, Ahmet Demir, Shiang Fang, Spencer L. Tomarken, Jason Y. Luo, Javier D. Sanchez-Yamagishi, Kenji Watanabe, Takashi Taniguchi, Efthimios Kaxiras, Ray C. Ashoori, and Pablo Jarillo-Herrero, “Correlated insulator behaviour at half-filling in magic-angle graphene superlattices,” *Nature* **556**, 80–84 (2018).
- [16] Yuan Cao, Valla Fatemi, Shiang Fang, Kenji Watanabe, Takashi Taniguchi, Efthimios Kaxiras, and Pablo Jarillo-Herrero, “Unconventional superconductivity in magic-angle graphene superlattices,” *Nature* **556**, 43–50 (2018).
- [17] Xiaobo Lu, Petr Stepanov, Wei Yang, Ming Xie, Mohammed Ali Aamir, Ipsita Das, Carles Urgell, Kenji Watanabe, Takashi Taniguchi, Guangyu Zhang, Adrian Bachtold, Allan H. MacDonald, and Dmitri K. Efetov, “Superconductors, orbital magnets and correlated states in magic-angle bilayer graphene,” *Nature* **574**, 653–657 (2019).
- [18] Leon Balents, Cory R Dean, Dmitri K Efetov, and Andrea F Young, “Superconductivity and strong correlations in moiré flat bands,” *Nature Physics* **16**, 725–733 (2020).
- [19] A. Uri, S. Grover, Y. Cao, J. A. Crosse, K. Bagani, D. Rodan-Legrain, Y. Myasoedov, K. Watanabe, T. Taniguchi, P. Moon, M. Koshino, P. Jarillo-Herrero, and E. Zeldov, “Mapping the twist-angle disorder and landau levels in magic-angle graphene,” *Nature* **581**, 47–52 (2020).
- [20] O A Tkachenko, V A Tkachenko, I S Terekhov, and O P Sushkov, “Effects of coulomb screening and disorder on an artificial graphene based on nanopatterned semiconductor,” *2D Materials* **2**, 014010 (2015).

- [21] O. P. Sushkov and A. H. Castro Neto, “Topological insulating states in laterally patterned ordinary semiconductors,” *Phys. Rev. Lett.* **110**, 186601 (2013).
- [22] Daisy Q Wang, Zeb Krix, Oleg P Sushkov, Ian Farrer, David A Ritchie, Alexander R Hamilton, and Oleh Klochan, “Formation of artificial fermi surfaces with a triangular superlattice on a conventional Two-Dimensional electron gas,” *Nano Lett.* **23**, 1705–1710 (2023).
- [23] C.-T. Liang, C. G. Smith, J. T. Nicholls, R. J. F. Hughes, M. Pepper, J. E. F. Frost, D. A. Ritchie, M. P. Grimshaw, and G. A. C. Jones, “Weak localization and electron-electron interactions in a two-dimensional grid lateral surface superlattice,” *Physical Review B* **49**, 8518–8521 (1994).
- [24] S. Melinte, Mona Berciu, Chenggang Zhou, E. Tutuc, S. J. Papadakis, C. Harrison, E. P. De Poortere, Mingshaw Wu, P. M. Chaikin, M. Shayegan, R. N. Bhatt, and R. A. Register, “Laterally modulated 2d electron system in the extreme quantum limit,” *Physical Review Letters* **92**, 036802 (2004).
- [25] Z. E. Krix, H. D. Scammell, and O. P. Sushkov, “Correlated physics in an artificial triangular anti-dot lattice,” *Phys. Rev. B* **105**, 075120 (2022).
- [26] L. Brey and H. A. Fertig, “Emerging Zero Modes for Graphene in a Periodic Potential,” *Physical Review Letters* **103**, 046809 (2009).
- [27] Zi-Dong Zhang, Cheng Cheng, Si-Yuan Yu, Ming-Hui Lu, and Yan-Feng Chen, “Electrically tunable elastic topological insulators using atomically thin two-dimensional materials pinned on patterned substrates,” *Phys. Rev. Appl.* **15**, 034015 (2021).
- [28] Xu-Chen Yang, Hongyi Yu, and Wang Yao, “Chiral excitonics in monolayer semiconductors on patterned dielectrics,” *Phys. Rev. Lett.* **128**, 217402 (2022).
- [29] Z. E. Krix and O. P. Sushkov, “Patterned bilayer graphene as a tunable strongly correlated system,” *Physical Review B* **107**, 165158 (2023).
- [30] Tommy Li, Julian Ingham, and Harley D. Scammell, “Artificial graphene: Unconventional superconductivity in a honeycomb superlattice,” *Physical Review Research* **2**, 043155 (2020).
- [31] Sayed Ali Akbar Ghorashi, Aaron Dunbrack, Ahmed Abouelkomsan, Jiacheng Sun, Xu Du, and Jennifer Cano, “Topological and stacked flat bands in bilayer graphene with a superlattice potential,” *Physical Review Letters* **130**, 196201 (2023).
- [32] Archana Mishra, S. R. Hassan, and R. Shankar, “Effects of interaction in the hofstadter regime of the honeycomb lattice,” *Physical Review B* **93**, 125134 (2016).
- [33] Peizhi Mai, Edwin W. Huang, Jiachen Yu, Benjamin E. Feldman, and Philip W. Phillips, *npj Quantum Materials* **8**, 1–7 (2023).
- [34] D. Q. Wang, D. Reuter, A. D. Wieck, A. R. Hamilton, and O. Klochan, “Two-dimensional lateral surface superlattices in gas heterostructures with independent control of carrier density and modulation potential,” *Applied Physics Letters* **117**, 032102 (2020).
- [35] Z. E. Krix and O. P. Sushkov, “Artificial graphene in a strong magnetic field: Bulk current distribution and quantum phase transitions,” *Phys. Rev. B* **101**, 245311 (2020).

Supplementary Information for Tuning the bandstructure of electrons in a two-dimensional artificial electrostatic crystal in GaAs quantum wells

Daisy Q. Wang,^{7,8} Zeb Krix,^{7,8} Olga A. Tkachenko,⁹ Vitaly A. Tkachenko,^{9,10} Chong Chen,¹¹ Ian Farrer^{a,11} David A. Ritchie,¹¹ Oleg P. Sushkov,^{7,8} Alexander R. Hamilton,^{7,8} and Oleh Klochan^{7,8,12}

⁷*School of Physics, University of New South Wales, Kensington, NSW 2052, Australia*

⁸*Australian Research Council Centre of Excellence in Future Low-Energy Electronics Technologies, The University of New South Wales, Sydney 2052, Australia*

⁹*Rzhanov Institute of Semiconductor Physics, Novosibirsk, 630090, Russia*

¹⁰*Novosibirsk State University, Novosibirsk, 630090, Russia*

¹¹*Cavendish Laboratory, J. J. Thomson Avenue, Cambridge, CB3 0HE, United Kingdom*

¹²*School of Science, University of New South Wales, Canberra, ACT 2612, Australia*

(Dated: February 21, 2024)

^a Present Address: Department of Electronic and Electrical Engineering, The University of Sheffield, Mappin Street, Sheffield, S1 3JD, United Kingdom.

MEASUREMENTS IN THE WEAK MODULATION REGIME

To access the very weak modulation regime, it is necessary to reduce the superlattice potential strength by using a deeper heterostructure. Details about the effect of the wafer depth on the strength of the superlattice potential are discussed in Supplementary section III. Here we show measurements performed on a device fabricated using a 37 nm deep heterostructure (W916) and show how the device can be continuously tuned from a plain 2DEG to an artificial crystal.

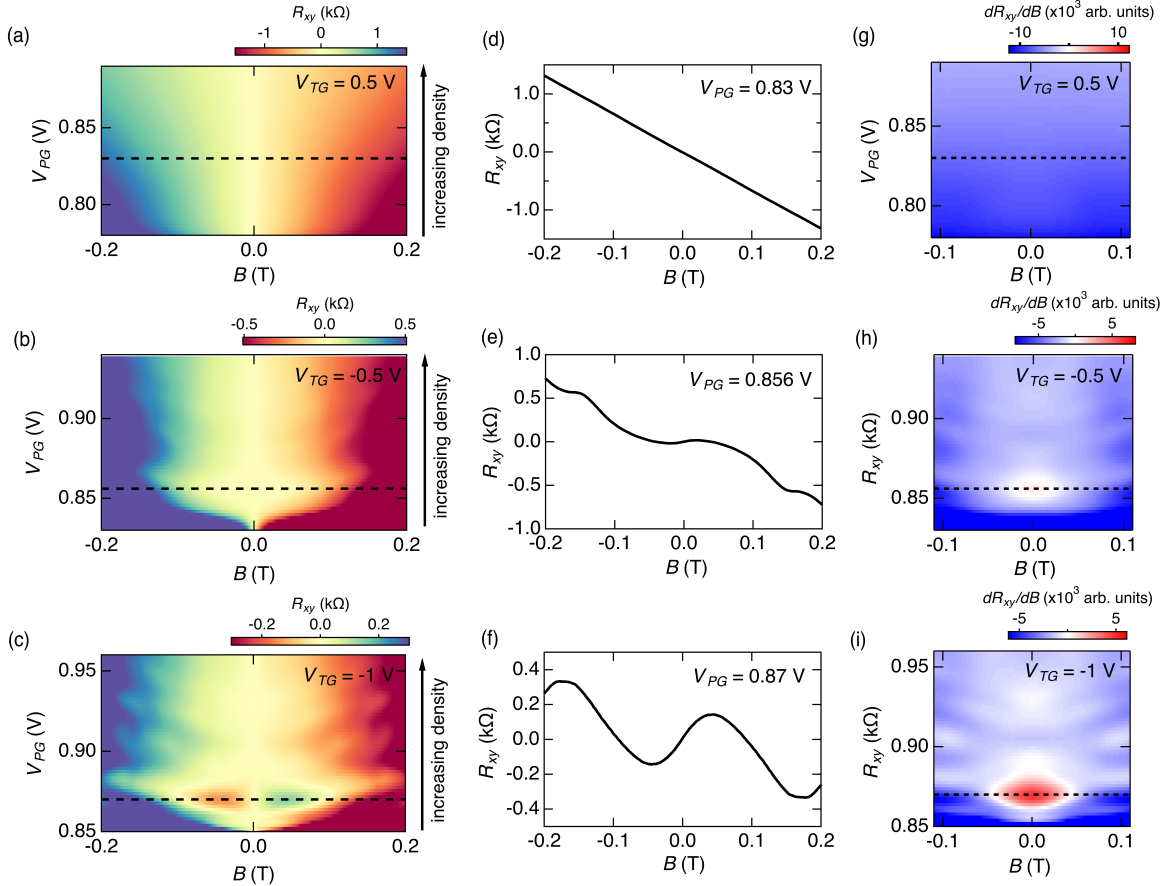


FIG. S1. Hall measurements of a device on the 37 nm deep heterostructure W916 with a lattice constant of 120 nm at $T = 1.5$ K. First column shows the evolution of Hall resistance as a function of the patterned gate voltage V_{PG} and perpendicular magnetic field B with increasing modulation strength (a) $V_{TG} = 0.5$ V, (b) $V_{TG} = -0.5$ V and (c) $V_{TG} = -1$ V. Dashed lines indicate the position of the linecuts for the second column. (d)-(f) Hall resistance as a function of B field at (d) $V_{PG} = 0.83$ V, (e) $V_{PG} = 0.858$ V and (f) $V_{PG} = 0.87$ V for three modulation strengths respectively, showing the change in Hall resistance near zero-field as the modulation strength is increased. (g)-(i) Hall coefficient as a function of as a function of V_{PG} and B at three different modulation strengths corresponding to (a)-(c). Red regions indicate where the Hall slope changes sign and the carrier type becomes hole-like.

In the regime of very weak modulation strength $V_{TG} = +0.5$ V, the system bears resemblance to a conventional 2D electron gas, as demonstrated by the featureless Hall resistance in Fig. S1(a),(d) and a negative Hall coefficient in Fig. S1(g). This slope is inversely proportional to the density of the 2D electron gas (2DEG) $n = 1/(edR_{xy}/dB)$, which in turn is directly proportional to the applied voltage on the patterned gate V_{PG} .

When the modulation potential is increased, by setting a top-gate voltage to $V_{TG} = -0.5$ V, we observe suppression of the Hall resistance around $B = 0$ (Fig. S1(b)). Increasing the potential modulation further to $V_{TG} = -1$ V causes the Hall resistance around $B = 0$ to change sign, as shown in Fig. S1(c,f). As a result, the Hall coefficient switches sign as highlighted by the red-colored region in Fig. S1(i), a direct signature of the existence of hole-like carriers. The periodic oscillations of the Hall resistance as a function of the magnetic field B seen in Fig. S1(f) are due to gauge invariance when integer numbers of flux quanta are threaded through each artificial unit cell, as discussed in the main text.

BANDSTRUCTURE EVOLUTION AS A FUNCTION OF MODULATION STRENGTH

As the modulation strength gradually increases by applying a more negative gate voltage on the top-gate, the mini-bands in the system gradually move apart and become separate. As the bands become discrete, more sign changes due to transitions between electron-like and hole-like carriers start to appear. On the other hand, as the modulation strength increases, we gradually lose transport in the first band and the sign changes in the first two graphene-like bands become suppressed. This is probably due to disorder in modulation potential and localization of electrons in the strong modulation regime. As shown in Fig. S2, at $V_{TG} = -0.5$ V, the first two graphene-like bands are fully developed with clear hole-like and electron-like regions observed both below and above the Dirac point. It is also worth noting that when the hole-like part of the second band overlaps with the third band, the Hall resistance can still have a positive slope due to the existence of both electron-like and hole-like carriers. This means the region of positive Hall slope above the second van Hove singularity can be larger than that corresponding to one band density since it contains overlapping bands. Only when the second band is fully separate from the third band, i.e. a bandgap has properly developed, the size of the positive Hall coefficient region above the first Dirac point can be used to calibrate the gate voltage for one band density in our system. As shown in Fig. S2(e)-(f), the band density n_0 of the system in V_{PG} is ~ 24 mV, which for a $a = 100$ nm triangular lattice, is equivalent to a 2DEG density of 2.3×10^{10} cm $^{-2}$ with 2 electrons per unit cell.

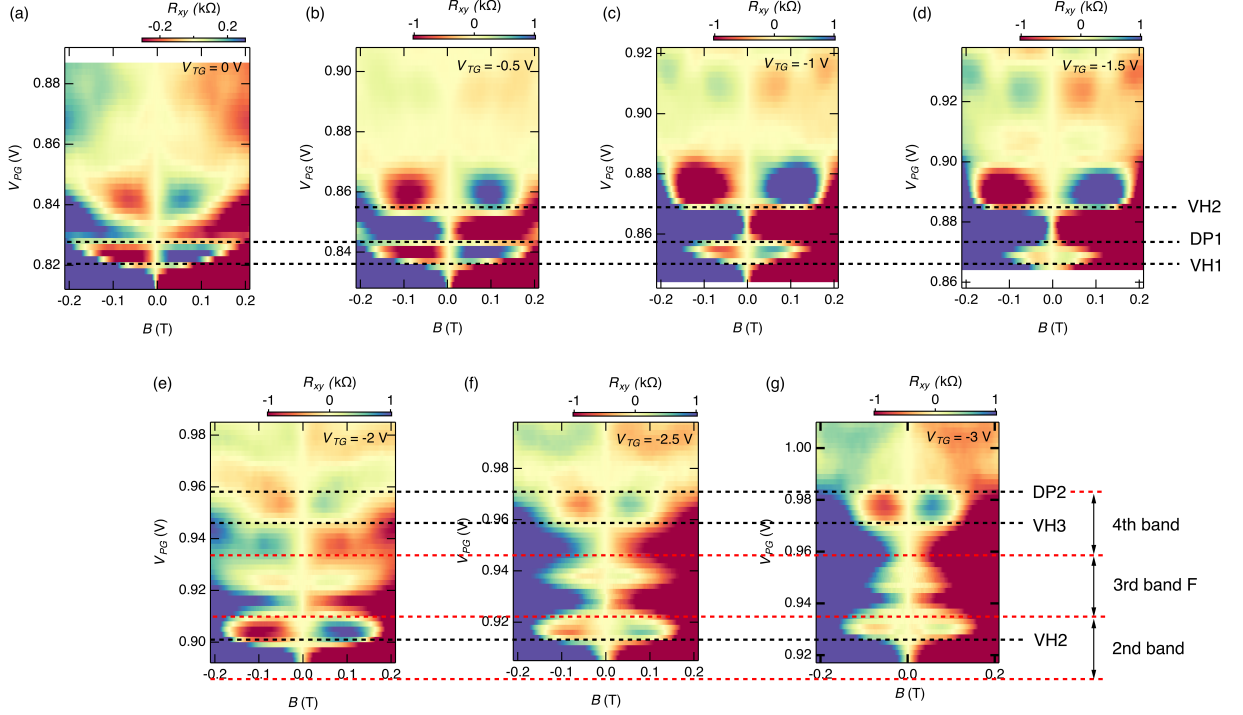


FIG. S2. Hall resistance R_{xy} as a function of patterned gate voltage V_{PG} and perpendicular magnetic field B for the device on 25 nm deep heterostructure W1740 with a lattice constant of 100 nm at $T = 1.5$ K. The modulation strength is gradually increased by stepping up the top-gate voltage V_{TG} (a) $V_{TG} = 0$ V, (b) $V_{TG} = -0.5$ V, (c) $V_{TG} = -1$ V, (d) $V_{TG} = -1.5$ V, (e) $V_{TG} = -2$ V, (f) $V_{TG} = -2.5$ V, (g) $V_{TG} = -3$ V. Black dashed lines indicate the positions of the Dirac points and van Hove singularities where Hall slope changes sign and/or the positions where each band terminates. Red dashed lines illustrate the evenly spaced bands in patterned gate voltage V_{PG} .

REPRODUCIBILITY ACROSS MULTIPLE DEVICES AND WAFERS

The strength of the modulation potential is predominantly determined by two experimental factors that are related to the device architecture and design: 1) the distance between the patterned gate and the 2DEG d and 2) the lattice constant a (see Ref. 20). When d is reduced, the modulation strength increases exponentially. Increasing a also increases potential modulation. However, a larger lattice constant results in a smaller band density which hinders the observation of the mini-bands. Therefore, the optimal range for the lattice constant is ~ 100 nm with a band density of $\sim 2 \times 10^{10} \text{ cm}^{-2}$ which is easily accessible in GaAs/AlGaAs heterostructures.

We have measured multiple devices on three different heterostructures: W1740 which is 25 nm deep (Figs in the main text and Fig.S2), W1735 which is 33 nm deep (Fig.S3) and W916 which is

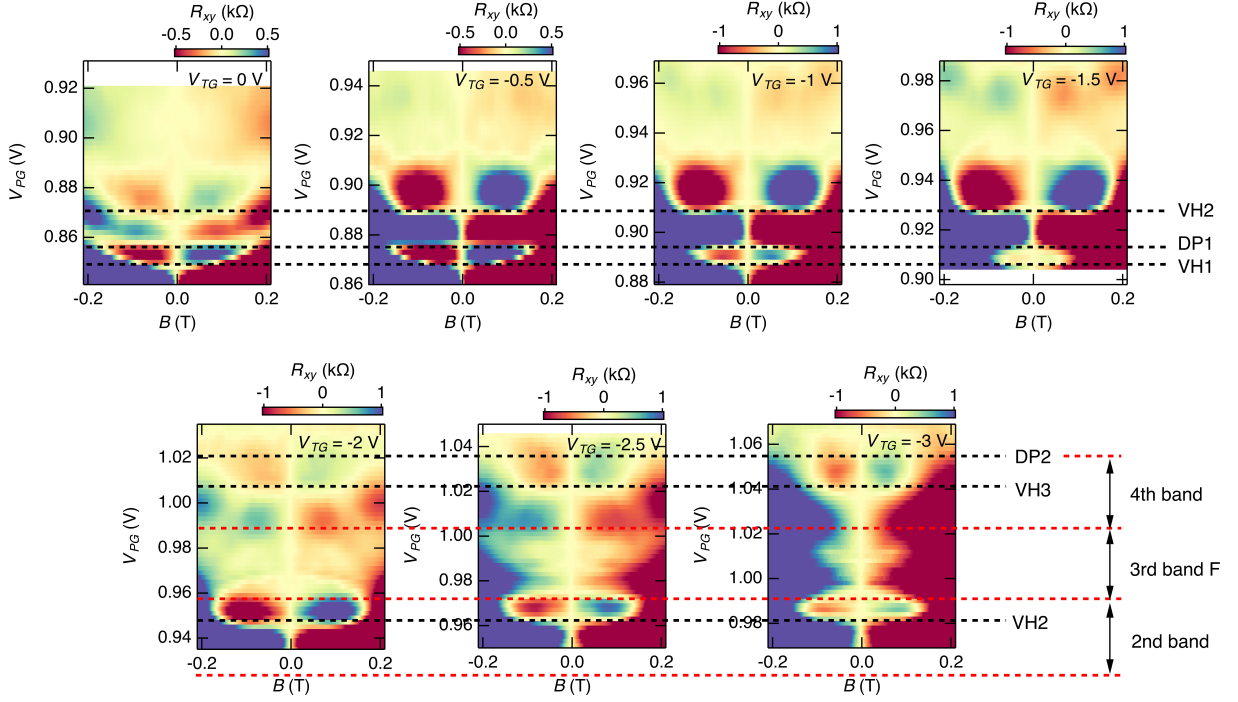


FIG. S3. Hall resistance R_{xy} as a function of patterned gate voltage V_{PG} and perpendicular magnetic field B for the device on 33 nm deep heterostructure W1735 with a lattice constant of 100 nm at $T = 1.5$ K. The modulation strength is gradually increased by stepping up the top-gate voltage V_{TG} : (a) $V_{TG} = 0$ V, (b) $V_{TG} = -0.5$ V, (c) $V_{TG} = -1$ V, (d) $V_{TG} = -1.5$ V, (e) $V_{TG} = -2$ V, (f) $V_{TG} = -2.5$ V, (g) $V_{TG} = -3$ V. Black dashed lines indicate the positions of the Dirac points and van Hove singularities where Hall slope changes sign and/or the positions where each band terminates. Red dashed lines illustrate the evenly spaced bands in the patterned gate voltage V_{PG} .

37 nm deep (Fig.S1 and Fig.S4). The devices on 25 nm and 33 nm deep wafers were made with a 100 nm lattice while the device on the 37 nm deep heterostructure has a 120 nm lattice. Even though the accessible range of modulation strength is different for different wafers, we still observe very similar behaviour across all devices. As shown in Fig.S2 and Fig.S3 we can extract a band width of $\Delta V_{PG} \approx 0.024$ V from the 25 nm deep device and a band width of $\Delta V_{PG} \approx 0.033$ V from the 33 nm deep device. This ratio of the two band widths in V_{PG} exactly reflects the change in depth by assuming a simple parallel capacitor model $\Delta V_{PG}/d \propto n_0 = 2.3 \times 10^{10} \text{ cm}^{-2}$.

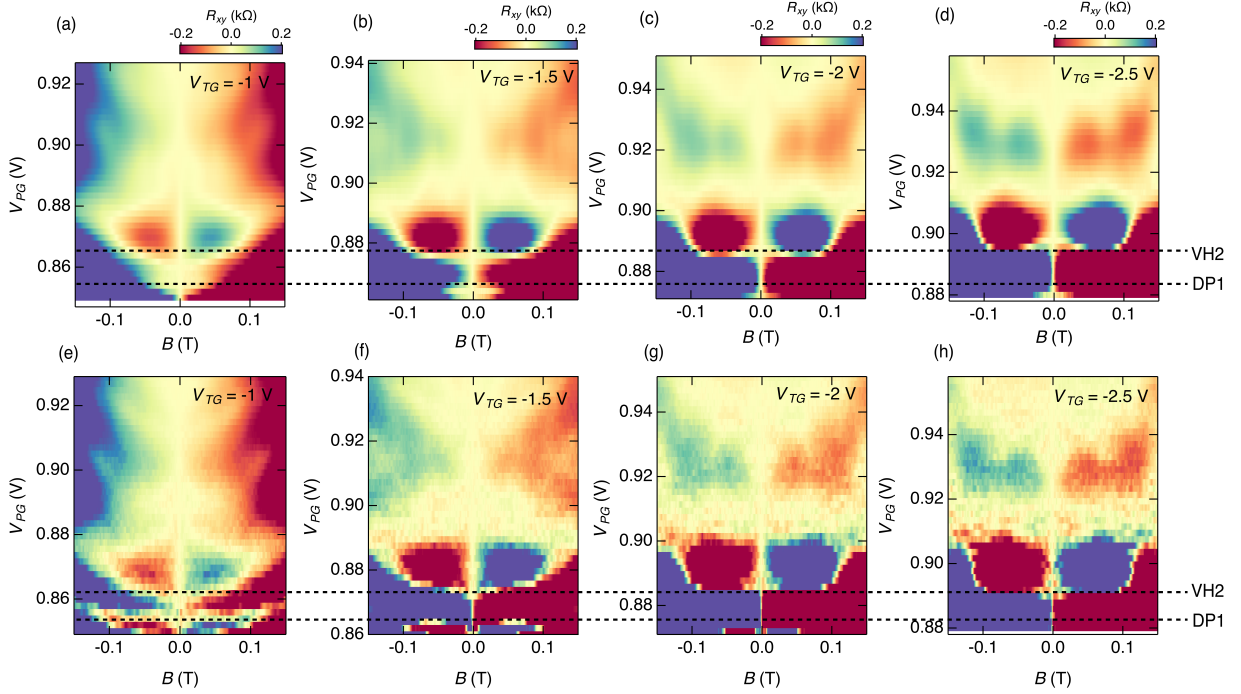


FIG. S4. Hall resistance R_{xy} as a function of patterned gate voltage V_{PG} and perpendicular magnetic field B for the device on 37 nm deep heterostructure W916 with a lattice constant of 120 nm. The top row (a,b,c,d) are measured at $T = 1.5$ K and the bottom row (e,f,g,h) are measured at $T = 20$ mK. Features related to the first Dirac point becomes more visible as the temperature is reduced. Modulation strength is gradually increased by stepping up the top-gate voltage V_{TG} : (a,e) $V_{TG} = -1$ V, (b,f) $V_{TG} = -1.5$ V, (c,g) $V_{TG} = -2$ V and (d,h) $V_{TG} = -2.5$ V. Dashed lines indicate the positions of the first Dirac point and the first van Hove singularity where Hall slope changes sign.

COULOMB SCREENING, EFFECT ON MODULATION STRENGTH

The actual potential (\tilde{U}) experienced by electrons differs from the applied potential (U_0) because of Coulomb screening. We can account for this difference using the Hartree equation

$$\tilde{U}_q = U_{0q} + \frac{2\pi e^2}{\epsilon q} n_q \quad (3)$$

Where n_q is the Fourier transform of the spatially varying particle density of a system described by Eqn.(1) in the main text with $U = \tilde{U}$. Here $\epsilon = 13$ is the dielectric constant of GaAs. The subscripts q denote Fourier coefficients. The Hartree equation must be solved at a particular Fermi energy, E_F . In real space, the particle density is defined by

$$n(r) = \sum_{\substack{k,n \\ E_{k,n} < E_F}} |\psi_{k,n}(r)|^2 \quad (4)$$

Where $\psi_{k,n}(r)$ are the Bloch functions obtained via numerical diagonalisation (see Methods). To solve the Hartree equation we assume that \tilde{U} , like U_0 , is sinusoidal, meaning that its only non-zero Fourier component is \tilde{U}_{g_i} . Evaluating the Hartree equation at $q = g_i$ we obtain

$$\tilde{W} = W_0 + \frac{2\pi e^2}{\epsilon g_i} \frac{n_{g_i}}{A_{cell}} \quad (5)$$

Where A_{cell} is the unit cell area in real space and

$$n_{g_i} = \int_{cell} d^2r n(r) e^{ig_i \cdot r} \quad (6)$$

Using Eqn. 5 we can find the strength of the applied potential W_0 necessary to obtain a self-consistent potential strength \tilde{W} . The results of this calculation are presented in Fig. S5. We remind that the parameter W is related to the peak-to-peak width U_{p-p} of the potential by $U_{p-p} = 9W$.

ESTIMATION OF MODULATION STRENGTH

Before we can estimate the potential amplitude a few points must first be made clear.

1. Potential amplitude decreases as electron density increases. For example, an imposed potential of $W_0 = 3$ meV is reduced to $\tilde{W} = 1$ meV when four energy bands are fully filled (at $n = 4n_0 = 9.2 \times 10^{10} \text{ cm}^{-2}$). This is the result of Fig. S5.
2. At large potential amplitudes each energy band is distinct, there is no overlap between bands. As the potential amplitude is reduced bands begin to overlap starting with the higher-energy bands first (see Figs. 1c-e in the main text).
3. If the bands of interest (the graphene-like and kagome-like bands) are distinct for a given imposed potential, W_0 , then there will be a ‘critical’ density n_c such that for all $n > n_c$ the energy bands are overlapping. This occurs because the potential strength decreases with density.

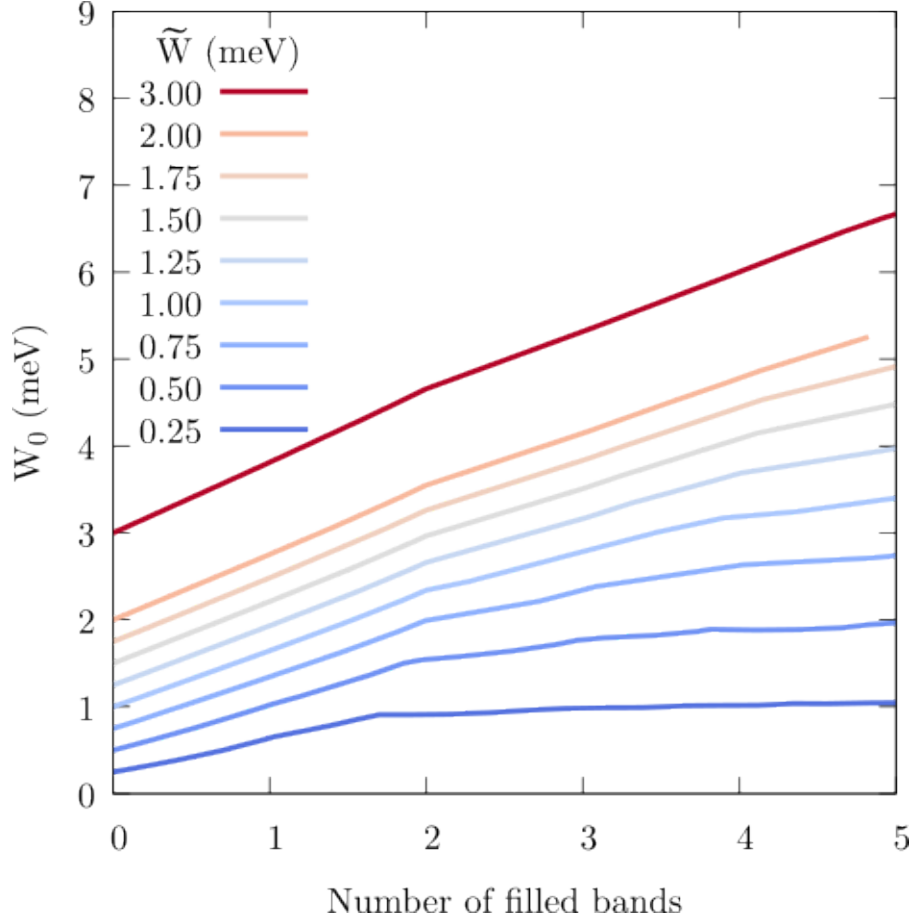


FIG. S5. Effect of Coulomb screening on the potential amplitude. Each curve is the applied potential W_0 necessary to obtain a given self-consistent potential \tilde{W} at different electron densities. Electron density is given on the horizontal axis in units of the number of filled electron bands. Each curve corresponds to a different value of \tilde{W} .

4. When the energy bands are distinct there is only ever one kind of charge carrier present for a given electron density (either electron-like or hole-like, see the inset to Fig. 1f in the main text). When the energy bands overlap both kinds of charge carrier can exist simultaneously. In the latter case no clear signature of the bands is expected in the Hall slope.

We use these points to estimate the size of the potential amplitude at $V_{TG} = -0.5$ V (Fig. 2) and $V_{TG} = -3$ V (Fig. 3). In particular, we identify the value of V_{PG} which corresponds to n_c . At voltages larger than this V_{PG} no Hall slope transitions are observed. We assign a value of \tilde{W} at this V_{PG} using our band structure calculation: the band structure must give the correct number of Hall slope transitions below n_c .

Starting with Fig. 2 we note that three transitions in the Hall slope are observed below $V_{PG} =$

0.87 V. Above $V_{PG} = 0.87$ V there are no further transitions. We identify the point $V_{PG} = 0.87$ V with the density n_c defined above. Using the notation defined in this section the band structure of Fig. 2d was computed for $\widetilde{W}(n_c) = 0.45$ meV. This band structure is consistent with the observed Hall slope transitions and with our estimation that the electron density is less than $n_0/2 = 1/A_{cell} = 1.15 \times 10^{10}$ cm⁻² at the lowest value of V_{PG} in Fig. 2a ($V_{PG} = 0.825$ V). Using Fig. S5 we find that the imposed potential amplitude must be $W_0 = 1$ meV.

We can repeat this analysis for the data in Fig. 3. In this figure the lowest value of V_{PG} corresponds to an electron density just above the first Dirac point. The first transition above this point corresponds to the second van Hove singularity ($V_{PG} = 0.927$ V). The next transition after this ($V_{PG} = 0.935$ V) is the top of the graphene-like bands. From the second transition point, the subsequent 0.024 V is identified with the third energy band (the flat band). Above the third band there are two further transitions in Hall slope. Again, the difference, ΔV_{PG} , between the top of the flat band and the second subsequent transition is 0.024 V. Each of these transitions, and the spacings between them are consistent with a potential amplitude $\widetilde{W} = 1$ meV at complete filling of four energy bands. At lower fillings the value of \widetilde{W} is larger (band structure shown in Fig. 3e). Using Fig. S5 we find that \widetilde{W} is 1.25 meV when three bands are fully filled and 1.75 meV when 2 bands are fully filled. Finally, the value of the imposed potential amplitude is $W_0 = 3$ meV. Note that in Fig. 3(c) we plot the bandstructure for $\widetilde{W} = 1.5$ meV which corresponds to a filling in the flat band region.

ESTIMATION OF DISORDER AND MOBILITY

There are 3 kinds of disorder in our device. (i) A short-range disorder related to the presence of impurities in the host semiconductor. (ii) A short-range disorder related to imperfections in nano-lithography process. (iii) A long-range disorder (puddles) related to imperfections in nano-lithography process. The disorder of kind (i) can be neglected because the host semiconductor is very clean, having a mobility of 500,000 cm²/Vs. Disorder of kinds (ii) and (iii) have been simulated numerically in detail in Ref. 20. It was shown that suppression of short wave-length harmonics due to the Poisson equation make type (ii) less important; puddle formation (type iii) is the most dangerous one, with the size of the puddles ranging from a few to several lattice periods. We thus concentrate on type (iii). First, we assume that puddles result in a Lorentzian broadening of the chemical potential

$$\frac{\Gamma/2}{\pi(\delta\mu^2 + \Gamma^2/4)}, \quad (7)$$

Using the width of the resistance peak at the first Dirac point DP1 we estimate the full-width-half-maximum Γ . Fig. S6 shows this peak at two temperatures, $T = 550$ mK and $T = 1.5$ K. The $T = 1.5$ K peak is slightly broader due to additional temperature broadening. To estimate the disorder broadening Γ we use the $T = 550$ mK data. If we take the base of the peak to be the resistance values at VH1 and VH2 then the full-width-half-maximum at this temperature is $\delta V_{PG} = 7.9$ mV. The difference in V_{PG} between VH1 and VH2 is 16 mV. Thus, the full-width-half-maximum δV_{PG} accounts for half of the change in electron density between VH1 and VH2. To translate this to an energy scale we take half of the energy difference between VH1 and VH2 in the computed bandstructure of Fig. 2d. Doing this we find

$$\Gamma = 0.2 \text{ meV} \quad (8)$$

Next, mobility is estimated using the standard equation

$$\mu = \frac{1}{n_{eff} e \rho_{xx}} \quad (9)$$

Where n_{eff} is the effective density of charge carriers and ρ_{xx} is resistivity. Note that both the chemical potential and the mobility are denoted by the same letter μ , we hope that the meaning of μ will be clear from its context. To estimate mobility near van Hove singularities VH1 and VH2 we have to remember that the effective density at the Dirac point is zero and the effective density at the van Hove singularities is about $n_e \approx n_0/4 = 5.7 \times 10^9 \text{ cm}^{-2}$. The measured longitudinal resistance presented in Fig. 2(g) and in Fig. S6 is about 2400 Ω ; to obtain resistivity we must multiply by the Van der Pauw constant $\frac{\pi}{\ln 2} = 4.53$, appropriate for a device with Van der Pauw geometry. Hence, $\rho_{xx} = 4.53 R_{xx} \approx 11,000 \text{ } \Omega$. The mobility close to VH1 and VH2 is about

$$\mu = 100,000 \text{ cm}^2/\text{Vs} \quad (10)$$

This has to be compared with the mobility of a free electron gas in GaAs at density $n_e = n_{eff} = 5.7 \times 10^9 \text{ cm}^{-2}$ which is about 10,000 cm^2/Vs .

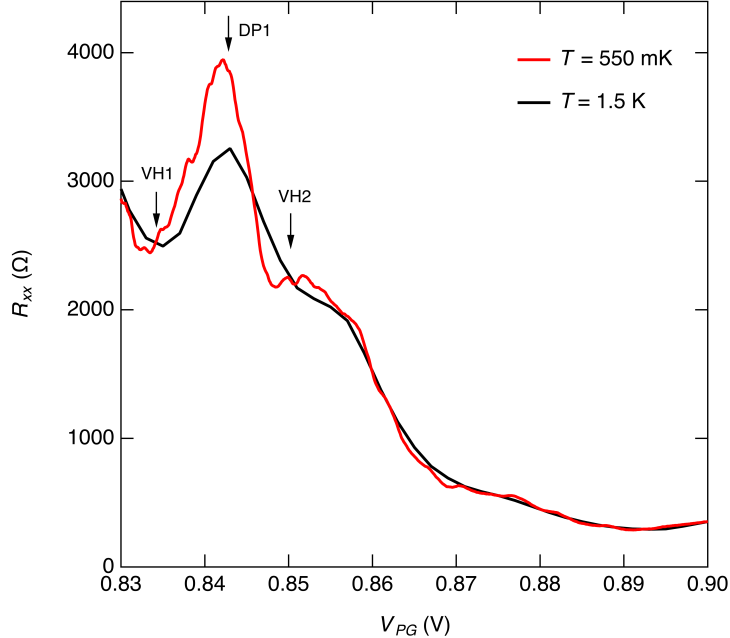


FIG. S6. R_{xx} as a function of V_{PG} at $V_{TG} = -0.5$ V. Two traces at different temperatures 1.5 K and 550 mK are plotted for comparison. The peak in R_{xx} corresponds to the same Dirac peak in Fig. 2 in the main text. Black arrows indicate the positions the Dirac point and van Hove singularities from the Hall measurement.

HOFSTADTER'S BUTTERFLY AND DENSITY OF STATES

To understand the results of Fig. 4 of the main text we computed the density of states of the simple Hamiltonian Eqn. (1) (Methods section) in the presence of a magnetic field. Using the gauge $\mathbf{A} = (0, Bx, 0)$ the Hamiltonian is

$$H = p_x^2/2m^* + (p_y - eBx)^2/2m^* + U(x, y) \quad (11)$$

The matrix elements of this Hamiltonian can be computed in the basis of Landau level eigenstates, given by

$$|k_y, n\rangle = e^{ik_y y} \chi_n(x - k_y/eB) \quad (12)$$

Where $\chi_n(x)$ is the n th wave-function of the harmonic oscillator with frequency $\omega = eB/m^*$. Using a method analogous to that used in the main text to address the zero-field limit, we take the matrix elements, $\langle k'_y, n | H | k_y, m \rangle$, and then numerically diagonalise. These matrix elements have a

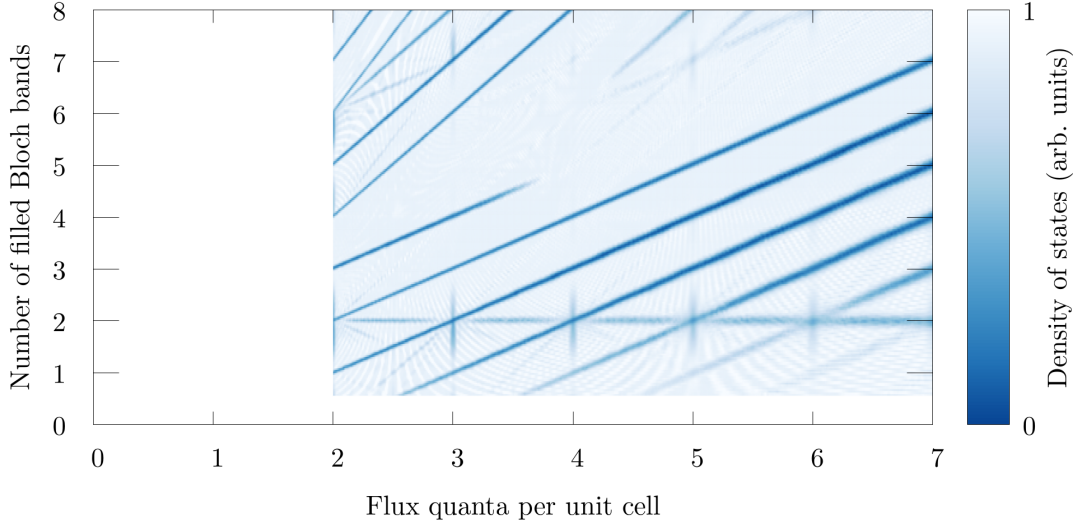


FIG. S7. Theoretical density of states at the Fermi energy (colour) as a function of particle density (expressed in units of $n_0 = 2/A_{cell}$, the particle density of a single Bloch band) and magnetic field (expressed in terms of the number of flux quanta per unit cell). To perform the calculation we suppose that the total particle density is independent of the magnetic field. The density of states is given in arbitrary units.

complicated form and have already been computed in previous works (see, for example, Ref. 35). Importantly, k_y can only be changed by $\pm 2\pi/a$ (see Ref. 35), so that we can set $k_y = k + j2\pi/a$ and $k'_y = k + i2\pi/a$ where k now varies from $-\pi/a$ to $+\pi/a$. To perform the numerical diagonalisation we must place restrictions on i, j and n, m such that $|i|, |j| < i_{max}$ and $n, m < n_{max}$. Again, the values of i_{max} and n_{max} are chosen such that all relevant energy levels are independent of them.

Using the explicit form for the matrix elements of Eqn. 11 given in Ref. 35, we can numerically diagonalise the Hamiltonian and obtain a set of energy levels, $\varepsilon_n(k)$. Here, n is a more general quantum number which encompasses both the traditional band index and the degrees of freedom normally enumerated by the quasi-momentum k_x . The strength of the magnetic field is a free parameter, so we can obtain a set of energy levels at each value of B that we wish to study. Strictly speaking, the magnetic field cannot become too small; at small fields the Landau level spacing becomes small and we must include more Landau level states in our basis. In other words, when B is too small n_{max} becomes too large for practical computations.

To compute the density of states we fix the total particle density n of the system; this will be independent of the magnetic field. Then, for each magnetic field B , we compute the total set of energy levels and find the energy μ such that number of states below μ gives the correct particle density n . After finding μ we compute the density of states in a small window around μ .

Our results for the density of states are plotted in Fig. S7. Here, we express magnetic field in terms of flux quanta per unit cell (for $a = 100$ nm one flux quantum corresponds to 0.475 Tesla). Particle density is expressed in terms of the number of filled Bloch bands (for $a = 100$ nm one filled band contains $n_0 = 2/A_{cell} = 2.3 \times 10^{10}$ cm⁻² states). In this figure the dark lines correspond to minima in the density of states, they appear when the chemical potential, μ , is within a band gap. We draw a connection between the parrallel lines observed in this figure (showing density of states) and in Fig. 4 of the main text (showing R_{xx}). Since these lines are parallel there are two associated periods: (i) the horizontal period $\Delta\phi/\phi_0 = 1$, and (ii) the vertical period $\Delta n/n_0 = 1$.